

Improving early detection of gravitational waves from binary neutron stars using CNNs and FPGAs

Ana Martins¹, Melissa Lopez^{2,3}, Gregory Baltus⁴, Quirijn Meijer^{2,3}, Marc van der Sluys^{†2,3}, Chris Van Den Broeck^{2,3}, Sarah Caudill^{§5,6}

¹ Institute of Theoretical Astrophysics, University of Oslo, Oslo, Norway

² Institute for Gravitational and Subatomic Physics (GRASP), Utrecht University

³ Nikhef – National Institute for Subatomic Physics, Netherlands

⁴ STAR Institut, Université de Liège, Liège, Belgium

⁵ Department of Physics, University of Massachusetts Dartmouth, Center for Scientific Computing

⁶ Data Science Research, University of Massachusetts Dartmouth, Dartmouth, USA

E-mail: a.i.s.martins@astro.uio.no

17 March 2025

Abstract. The detection of gravitational waves (GWs) from binary neutron stars (BNSs) with possible telescope follow-ups opens a window to ground-breaking discoveries in the field of multi-messenger astronomy. With the improved sensitivity of current and future GW detectors, more BNS detections are expected in the future. Therefore, enhancing low-latency GW search algorithms to achieve rapid speed, high accuracy, and low computational cost is essential. One innovative solution to reduce latency is the use of machine learning (ML) methods embedded in field-programmable gate arrays (FPGAs).

In this work, we present a novel WaveNet-based method, leveraging the state-of-the-art ML model, to produce early-warning alerts for BNS systems. Using simulated GW signals embedded in Gaussian noise from the Advanced LIGO and Advanced Virgo detectors' third observing run (O3) as a proof-of-concept dataset, we demonstrate significant performance improvements. Compared to the current leading ML-based early-warning system, our approach enhances detection accuracy from 66.81% to 76.22% at a 1% false alarm probability. Furthermore, we evaluate the time, energy, and economical cost of our model across CPU, GPU, and FPGA platforms, showcasing its potential for deployment in real-time gravitational wave detection pipelines.

† The research leading to these results has received funding from the European Union's Horizon 2020 Programme under the AHEAD2020 project (grant agreement No. 871158). This publication is part of the project Cortex with project number 00686766 of the research programme NWA which is (partly) financed by the Dutch Research Council (NWO).

§ S.C is supported by the National Science Foundation under Grant No. PHY-2309332.

1. Introduction

In recent years, Astrophysics and adjacent sciences have been expanding at an astronomical pace. A significant driver of this growth is the detection of gravitational waves (GWs), which are ripples in spacetime generated by astronomical cataclysms. In September 2015, the Laser Interferometer Gravitational-Wave Observatory (LIGO) [1] and Virgo [2] collaborations confirmed the existence of GWs by detecting a binary black hole (BBH) merger [3]. Since then, over 90 confident events have been detected in the past three observation runs by LIGO-Virgo collaboration [4, 5, 6, 7]. Among these astronomical events, only two binary neutron star (BNS) mergers were detected [8].

As GW detectors become increasingly sensitive with each upgrade, the enhanced capabilities of second-generation detectors and the future third-generation detectors, such as the Einstein Telescope (ET) [9], Cosmic Explorer [10] or the space-based Large Interferometer Space Antenna [11], will allow for more frequent detection of binary neutron star (BNS) mergers and other exotic systems. Nonetheless, this increase in sensitivity comes at increase in computational complexity, as more sources will be detected. In the era of ET, it is estimated that $8 \times 10^4 \text{ yr}^{-1}$ BBH [12] and $7 \times 10^4 \text{ yr}^{-1}$ BNS [13] will be detected, which could lead to over 400 daily GW merger events, as well as the detection of other exotic sources [14]. Moreover, while BNS GW signals are detectable for seconds with current detectors, they will be present for hours in the ET era.

The current state-of-the-art for detecting modelled GW signals, known as matched-filtering—a technique based on cross-correlating models, or templates, with GW detector data [15, 16, 17, 18, 19]—has led the LIGO-Virgo-KAGRA collaboration to develop several low-latency matched-filtering pipelines for producing real-time GW alerts [20, 21, 22, 23, 24]. While these methods have been successful, matched-filtering techniques are known to be computationally intensive, posing challenges for future detectors and negatively affecting the environment [25].

In recent years, machine learning (ML) techniques have gained significant interest due to their success in various tasks and domains [26]. A key advantage of ML is its fast inference, with most computations occurring during the training stage. This is crucial for GW searches, particularly for early warning of BNS GW signals in multi-messenger astrophysics. The goal is to detect GW signals during the inspiraling phase, where both neutron stars are orbiting around each other, before they merge into a more massive astronomical object (known as merger phase), to enable electromagnetic telescope follow-ups. This task is challenging because GW signals are often buried in detector noise, with the signal being weaker during the inspiral phase and strengthening as it approaches the merger.

GPUs, widely used for deploying ML algorithms, are well-known for being costly, consuming large amounts of energy, having short lifetimes and potentially introducing high latencies within data transfer. In a low-latency framework, these characteristics could hamper the early detection of GW signals. An interesting alternative is to embed

ML algorithms in field-programmable gate arrays (FPGAs). FPGAs show promise by having longer lifetimes and being more energy-efficient than state-of-the-art hardware. Furthermore, high-end FPGAs are faster than CPUs and GPUs [27], and low-end FPGAs are more affordable than CPUs or GPUs in the same tier. We choose the latter to explore their applicability and limitations.

In this work, to build more sustainable and environmentally-friendly alternatives, we explore the performance of FPGAs with respect to GPUs and CPUs to detect the early inspiral of BNS GW signals with ML-based algorithms^{||}. This paper is structured as follows: in Section 2, we address the state of the art in early warning with ML-based methods and motivate the need to improve the precision at a limited computational cost; in Section 3, we describe the input data; in section 4, we describe the hardware employed and ML architectures, as well as learning and quantization strategies (reduction from floating-point to fixed-point representation); in Section 5, we present the main findings of this work, comparing our model with the state of the art in terms of accuracy and computational cost; finally, Section 6 presents the conclusions of this research with avenues for future research.

2. Related work

The challenges in GW research require innovative solutions, and ML has emerged as a crucial tool for addressing them due to its adaptability and transversality. In the past few years, researchers have explored different ML applications to GW data analysis, such as detection of modelled [28, 29] and unmodelled GW signals [30, 31, 32, 33, 34, 35], non-transient burst noise characterization [36, 37] and synthetic data generation [38, 39, 40, 41], among others. Refer to [42] for a review.

Traditional GW searches use the inspiral part of the waveform, as early efforts have shown that it is possible to detect a signal with only a fraction of the waveform model with matched-filtering techniques [20]. The first early warning ML-based algorithm implemented `ResNet50` [43] training on spectrograms containing solely the inspiral part of the waveform [44]. However, as noted in [45], this added pre-processing step slows the inference by ~ 0.5 s. To address this, [45] suggested using GW detector time series in design sensitivity, and employing 1-dimensional convolutional neural networks (CNNs), eliminating the need for this pre-processing step and enhancing efficiency. This proof of concept work led to subsequent efforts in this line of research [28, 29, 46, 47, 48, 49].

In particular, [29], building on the previous work of [45] and [28], extended this method to the simulated noise of third and fourth observing runs (O3 and O4), as well as real O3 data. While [29] is the current state of the art, some of the limitations of this study are described below:

- **Large number of trainable parameters:** The fixed input-signal of this work has a duration of 300 s with a sampling frequency of 512 Hz, resulting in 155,648 data

^{||} The code is accessible in GitHub: <https://github.com/anaismartins/deploying-custom-nn-in-fpga>

points. Due to the long size of the input, large and complex models, that could lead to higher accuracy, would not fit into the device’s memory.

- **Catastrophic forgetting:** This investigation successfully implements curriculum learning –where the model learns easier examples to then transition to harder ones– by lowering the maximum frequency of the signals or rather detecting the signal earlier. However, it is observed that the model forgets easier steps of curriculum learning due to its over-fitting.
- **High false positive rate:** The model has a large number of false positives, i.e. misclassifying detector noise as GW signal, regardless of its decision threshold.

To overcome the limitations of the previous work, hereafter referred to as `FindCNN`, we implemented an algorithm inspired by `WaveNet` [2016arXiv160903499V] named `GWNet`. Similarly to [50] and [33], this choice was motivated by the similitude between GW time series data and audio or speech signals. For a fair comparison, we reproduced `FindCNN` and trained and tested both models on the same simulated GW detector data.

FPGAs have been used for ML applications [51], also in high-energy physics [52, 53]. We highlight the pioneering work in [54] for the implementation of recurrent neural networks for anomaly detection in GW. As added value, in this work we evaluate the performance of the `FindCNN` and `GWNet` models in CPU, GPU and FPGA devices, as well as their time, energy consumption and economical cost.

3. Data set and pre-processing

A GW search algorithm processes raw detector data, producing a score about whether it contains a GW signal. We can find GWs using supervised learning, where we distinguish detector noise (called a negative class) from detector noise plus GW signal (called a positive class).

In a real scenario, the negative class is much larger than the positive class, as only ~ 100 GW signals have been discovered at the present date. Thus, it is required to simulate GW signals, adding them to detector noise. This process is commonly referred to as “injections”, and they will be the positive class of this study. Hence, we construct a balanced data set of samples with only detector noise (negative class), and injections (positive class). Simulated Gaussian noise is generated with the average power spectral density of the third observing run (O3) for Hanford, Livingston and Virgo[¶].

As proposed in [29], to encompass all potential BNS systems, the component masses are uniformly distributed $\in [1, 3] M_{\odot}$, and the waveform approximant *SpinTaylorT4* [57] (used to model inspirals) was chosen. Moreover, the sources are uniformly distributed over the sky, including spin effects.

[¶] We use the PyCBC package [55]. In particular, the power spectral densities `aLIGOaLIGO140MpcT1800545` and `aLIGOAdV03LowT1800545`, an average of O3, respectively for the Advanced LIGO and Advanced Virgo detectors [56]. Refer to https://gwosc.org/03/o3_details/ for technical details of the observing run.

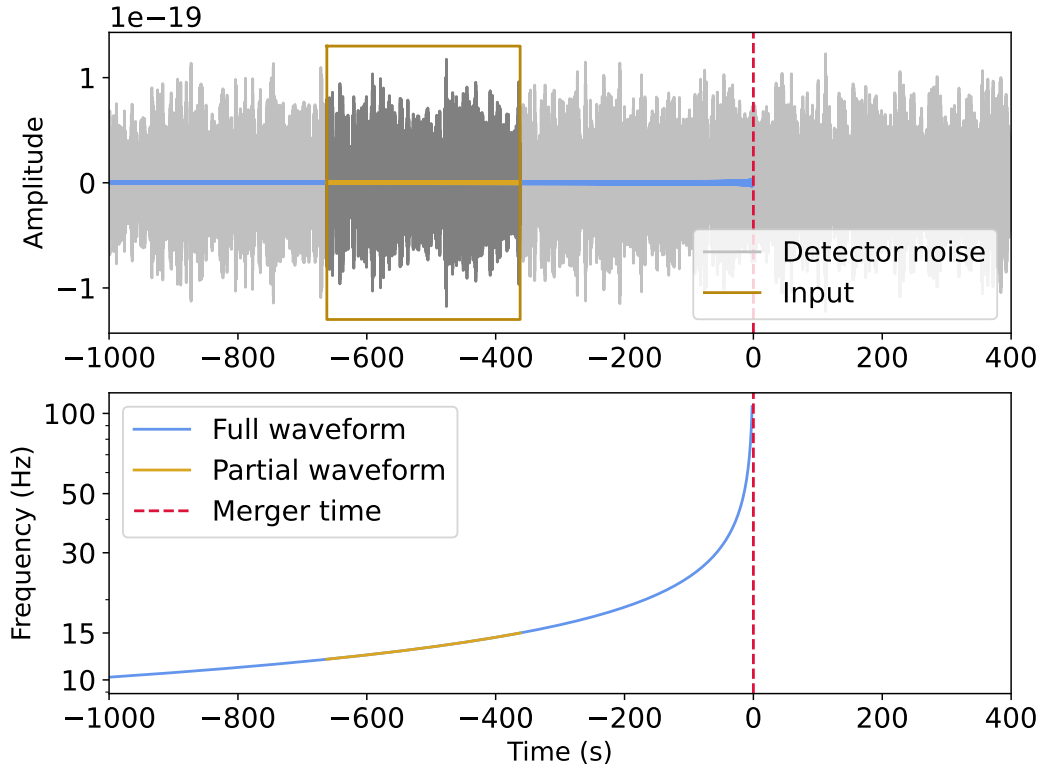


Figure 1. (Top) Representation of the inspiral phase, where both neutron stars are orbiting around each other, of a GW signal (blue) buried in simulated raw LIGO noise (grey). The vertical red line indicates the merger time. The GW waveform was modelled using *SpinTaylorT4*-which only models the inspiral phase-with progenitor masses ($m_1 = 1.46 M_\odot$, $m_2 = 1.27 M_\odot$), similar to GW170817. The input to the ML model is contained within the yellow rectangle, i.e. 300 s of data sampled at 512 Hz. (Bottom) Frequency evolution of the full GW waveform (blue) and the partial waveform (yellow).

As GWs have a weak amplitude, they are hard to distinguish from detector noise. For illustration, in Fig. 1 (top panel) we show the GW inspiral of a signal similar to GW170817 [8] in raw Advanced LIGO detector noise. To highlight its amplitude a common practice is to filter the data between 10 and 100 Hz, and whiten it, i.e. make the signal Gaussian-like with uniform variance by removing all the correlation of the noise [58]. Afterwards, we normalize the data $\in [-1, 1]$. As we can observe in Fig. 1, the inspiral phase lasts several minutes, so, as in [29], we pre-select 300 s of data. In the bottom panel, we show the relation between time and frequency of the source. Because of this relation, the difficulty of the input is governed by the maximum frequency f_{max} within a time window. Samples with higher (lower) f_{max} will be closer (further) to the merger, meaning that they will be detected later (earlier).

As the Hanford, Livingston and Virgo observatories measure GW signals independently, a signal that appears simultaneously in data from multiple detectors at the same time is more likely to be of astronomical origin. From an ML perspective,

independent detector data is input as separate channels.

4. Methodology

In this work, we do not only aim to detect GW signals as early as possible, going down in frequency f_{max} , but also to minimize the number of false positives (FP), to avoid sending false alerts to electromagnetic telescopes. Thus, we have developed a WaveNet-like architecture, **GWaveNet**, that we compare to the current state of the art, **FindCNN**. In the following sections, we describe the hardware employed for the deployment of the models and provide an overview of **FindCNN** and **GWaveNet**.

4.1. Hardware specifications

The manufacturing and use of state-of-the-art hardware are causing substantial damage to the environment and this is only predicted to increase, with most emissions from data-center equipment being related to manufacturing [59] and computation energy predicted to hit the world’s energy production capacity by 2040 [60]. In this context, it is of interest to understand the computational cost of low-latency algorithms of large physics experiments, such as Advanced LIGO-Virgo detectors, as well as their lifetime under heavy usage. In the following, we provide the specifications of the hardware employed in this work.

- **CPU:** We use the AMD EPYC 7551P 32-Core Processor [61], which has an expected lifetime of around 5 to 10 years. We used the full 32 cores for testing.
- **GPU:** We used the NVIDIA Tesla V100 [62] for training and validation, and NVIDIA GeForce GTX 1080 [63] for testing and energy consumption calculation. Their expected lifetime is around 3 to 5 years.
- **FPGA:** We use the AMD Kria KV260 Vision AI Starter Kit [64]. Its expected lifetime is around 10 to 15 years. We use the most recent and fastest pre-made architecture for this system-on-chip, B4096, with 4096 peak operations per cycle. Furthermore, we use 10 threads for testing, which we found to be the optimal amount.

At the time of their launches, the CPU and GPU used for inference were nine and three times more expensive than the FPGA used in this study. As of the current date of this investigation, the NVIDIA GeForce GTX 1080 GPU is eight years old, and the AMD EPYC 7551P is seven years old, with both considered obsolete. Typically, CPUs and GPUs become outdated even before their lifespan ends, as they struggle to compete with newer devices. In contrast, FPGAs are customizable, allowing modifications to keep them competitive throughout their lifetime. Consequently, the carbon footprint of using FPGAs is significantly lower than that of traditional processing units, not only because they consume less energy during operation but also due to their extended effective lifespan.

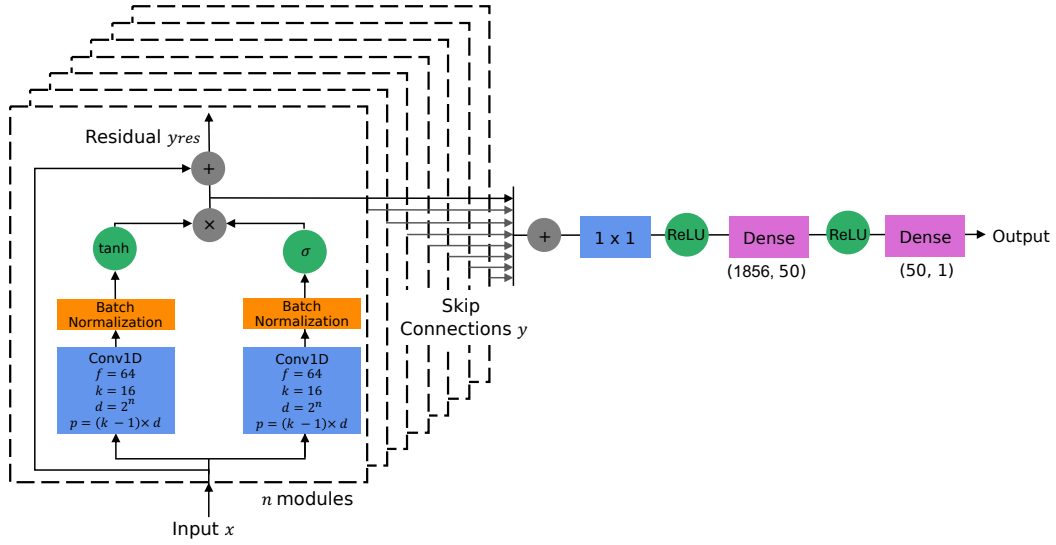


Figure 2. Overview of the modified **WaveNet** convolutional architecture for a single data stream, adapted from [65]. We present $n = 7$ 1-dimensional **WaveNet** modules composed of dilated causal convolutions (blue) with the number of filters f , kernel size k , dilation d and padding p , batch normalization layers (orange), tanh and sigmoid σ activations (green). Furthermore, we show 1×1 convolutions (blue), dense layers (pink), and ReLU and Softmax activations (green).

4.2. Basic components

4.2.1. Common details We implemented **FindCNN** and **GWaveNet** using the PyTorch package [66]. Both networks minimize the binary cross-entropy (BCE) loss in PyTorch, the *BCEWithLogitsLoss* i.e., Sigmoid activation integrated with BCE loss [67]. We decided to employ this loss instead of *BCELoss* since it is more numerically stable. Note that the original **FindCNN** [29] uses *BCELoss* instead.

4.2.2. *FindCNN* It is a 1-dimensional CNN [29] that starts with a batch normalization layer [68], to stabilize and accelerate the training process, followed by 5 convolutional blocks and two dense layers. The convolutional blocks are composed of a convolutional layer with stride 4, a ReLU activation function [69], and a MaxPooling layer [70] with stride 1. Each convolutional layer has successively kernel sizes k [16, 8, 4, 8, 16], and number of filters f [32, 64, 128, 256, 256]. This structure allows capturing high-level features at earlier layers while capturing finer details at intermediate layers. Furthermore, the combination of large kernel k and large filters allowed the last layers to capture high-level context with great expressiveness. Despite the compression of the input due to the usage of large kernel sizes k , the first dense layer is one of the most expensive ones, as it further compresses an input of 37,632 data points to only 128. This model has 6,179,303 trainable parameters, mainly due to the length of the input and large dense layers.

4.2.3. *GWaveNet* **WaveNet** is an expressive CNN designed for the generation of high-fidelity speech audio [65]. The architecture is capable of handling long-range temporal dependencies, a characteristic desirable for GW data analysis, and in particular for BNS searches, due to their long inspirals. **WaveNet**-like models have been previously implemented in the field of GW searches [33, 50]. These implementations modify **WaveNet** for binary classification. This is a common point in the current investigation. However, previous **WaveNet** models were constructed as an ensemble with non-causal dilated convolutions, while we encode the information of all detectors in a single model with causal dilated convolutions.

Causal dilated convolutions combine the power of dilation [65], which allows the NN to capture a larger context without increasing the computational load significantly, and causal convolutions, to effectively learn the time ordering of the data. Our experiments showed an improved performance when obeying the arrow of time with causal convolutions. These convolutions are encapsulated in **WaveNet** modules.

We present the full architecture of **GWaveNet**, including the **WaveNet** modules in Fig. 2. We can observe how an input x gets duplicated and each copy gets fed into a causal convolution block (blue), followed by a batch normalization layer (orange). Then, one output passes a tanh activation function (green), while the other passes a Sigmoid σ activation function (green). This is known as gated activation [71], designed for capturing complex relations in sequential data. Afterwards, the two outputs are multiplied (grey), generating the output of the module, y . At this point, the initial input x is added to the output y to form the residual input y_{res} that passes to the next module. On the other hand, the output y is sent towards the final output of the network that will feed the *BCEWithLogitsLoss*. Before this step, all the y outputs of the modules are summed, passing a 1×1 convolution (blue) and two dense layers (pink) with ReLU activation functions (green) [69]. It is relevant to note that original **WaveNet** modules used 1×1 convolutions in between each module for further compression, but due to the fixed number of filters f , this was not needed.

GWaveNet is composed of 7 **WaveNet** modules with kernels $k = 16$, number of filters $f = 64$ and dilation $d = 2^i$ for $i \in [0, \dots, 6]$. Because of this, the modules are highly expressive, having large receptive fields, which allows the compression of the input from 155,648 to 2,496 data points and 64 filters. Using a 1×1 convolutional layer allows further compression of the first dense layer: now it needs to compress an input of 2,496 to 50 data points. Thus, the number of trainable parameters of **GWaveNet** is 522,598, 12 times fewer parameters than **FindCNN**.

4.3. Learning strategy

As we mentioned in Sections 2 and 3, [29] implemented a curriculum learning strategy going down in maximum frequency f_{max} . For this aim, five data sets with different average f_{max} are built (see Table 1). In this way, the model first learns easier examples, closer to the merger, and slowly transitions to harder examples, further from the merger.

Each data set is composed of 22,600 samples for both classes, such that for each curriculum learning step we use 71% for training, 9% for validation and 20% for testing.

In GW data analysis, it is common to measure the loudness of the signal in terms of signal-to-noise ratio (SNR) [19]. However, [28] and [29] introduced the concept of partial inspiral signal-to-noise ratio (PISNR) to describe the corresponding SNR of the partial waveform, seen by the CNN. Thus, we use this magnitude for comparison (Table 1).

Data set	f_{min} (Hz)	f_{max} (Hz)	SNR	PISNR
D_1	12.9	40.0	100.3	34.5
D_2	12.8	35.0	127.2	342
D_3	12.6	30.0	186.5	34.7
D_4	12.3	25.0	344.6	34.7
D_5	11.7	20.0	1161.4	34.6

Table 1. In this classification task the positive class is a GW simulated signal added in raw detector noise. To enhance the learning we create five curriculum learning data sets D . In this table, we present the most relevant magnitudes of the GW simulations for each curriculum learning data set: the averages of the minimum frequency f_{min} , the maximum frequency f_{max} , the network (Hanford, Livingston and Virgo) SNR and the PISNR.

To avoid catastrophic forgetting, we use a progressive curriculum learning approach, where the training set \mathcal{D}_T and validation sets \mathcal{D}_V are defined as

$$\mathcal{D}_k \equiv \bigcup_{i=1}^k \mathcal{D}_i, \quad (1)$$

Here, \cup denotes the set union of the data, and the curriculum step is $k = \{1, 2, 3, 4, 5\}$. Each curriculum step in `FindCNN` lasts 6 epochs, minimizing a weighted *BCEWithLogitsLoss* to lower the number of FPs, i.e. it is more relevant to correctly classify the noise class (negative class) than the injection class (positive class) to avoid false alerts. Thus, as in the original work, we weigh the injection class by 0.4. Regarding the optimizer, we employ AdaMax [72] with a weight decay of 10^{-5} and the learning rate is 8×10^{-5} .

While `GWNet` has less trainable parameters than `FindCNN`, it is quite a complex model. To control the overfitting of the model we employ an early stopping algorithm where the curriculum step stops early if

$$|\mathcal{L}_{val}^e - \mathcal{L}_{val}^{e^{\text{best}}}| < \epsilon, \quad \text{given } e - e^{\text{best}} \geq n, \quad (2)$$

where \mathcal{L}_{val}^e represents the validation loss of the current epoch e , $\mathcal{L}_{val}^{e^{\text{best}}}$ is the validation loss of the best epoch e^{best} , ϵ the tolerance and n the patience. Too small a tolerance gives way to overfitting and too high a tolerance does not let the NN reach its full potential, favouring underfitting, and the opposite goes for the patience. After several

experiments we set $\epsilon = 10^{-4}$ and $n = 2$, which proved to be good trade-off values. Moreover, for each curriculum step, we select the weights of the best-performing epoch, i.e. the one with the lowest validation loss, as initialization for the next step. We also employ *BCEWithLogitsLoss* weighted at 0.1. After several experiments, the AdamW optimizer [72] showed the best performance. Furthermore, we use an adaptive learning rate to allow the network to learn more slowly at more difficult steps: given an initial learning rate $lr_0 = 2 \times 10^5$, at each curriculum step $c \in [1, 5]$, we set $lr_c = lr_0/c$.

4.4. Modified architectures and quantization

In this work, we used the AMD Kria KV260 Vision AI Starter Kit [64], and the Vitis AI software [73] for the deployment of the models. As Kria KV260 is designed for vision applications, it is only prepared to deal with 2-dimensional operations. Hence, to run the models in the chosen FPGA, we transformed the 1-dimensional **FindCNN** and **GWaveNet** to 2-dimensional versions: **FindCNN2D** and **GWaveNet2D**. Nonetheless, in a low-latency context, this implies reshaping within the FPGA, but such operation is not supported to run on the data processing unit (DPU), needing to be run in the non-optimized CPU of the FPGA.

Further modifications were performed to maximize the number of layers that could run on the DPU. For **FindCNN**, we added a 1×1 convolution at the end of the convolution blocks to cut the number of filters in half. On the other hand, **GWaveNet** required more changes: we moved from constant to the supported replicate padding, we changed the traditional tanh and σ activations to linearized versions, we reduced the kernels size k from 16 to 2, to allocate the model in memory and we lowered the number of filters in the sixth module to 32. This last step forced us to add a 1×1 convolutional layer after each **Wavenet** module to reduce the number of filters of each block's output to 32. However, despite these changes, at the end of the day, no versions of **GWaveNet** could be compiled in the DPU IP because of software limitations.

Last but not least, due to the limited memory of FPGAs, it is necessary to quantize our models, transforming the model's weights from floating point to lower bit-widths to save memory and accelerate inference. In this work, we use the power-of-two quantization [74], which is a robust logarithm-based quantization strategy implemented in Vitis AI [75].

5. Results

5.1. Performance

In Section 3, we mentioned that the input data has 155,648 data points and three channels, corresponding to Hanford, Livingston and Virgo, that we use to train, validate and test both models. In Fig. 3, we present the losses (solid line) and accuracies (dashed line) for **FindCNN** (top panel) and **GWaveNet** (bottom panel) for training (blue) and validation (yellow). For this figure, we use a decision threshold of 0.5 to calculate the

accuracies, i.e. the cutoff value used to distinguish the classes is 0.5. The progressive curriculum learning step is shown by vertical dotted lines, where at each step we add samples further away from the merger. Furthermore, we mark the best-performing epoch from each curriculum learning step in red, i.e. the epoch with the best validation loss.

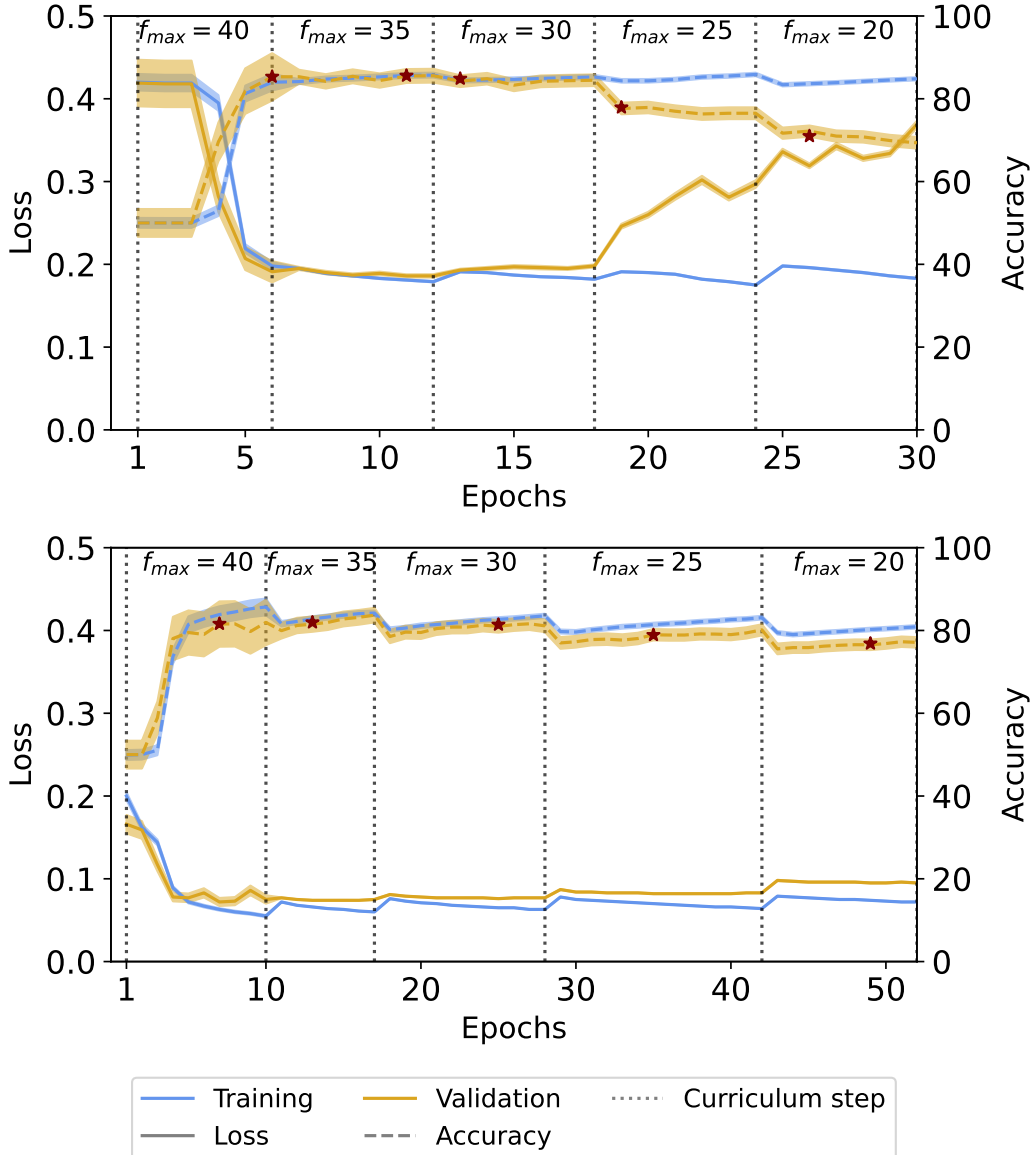


Figure 3. Training and validation of FindCNN (top) and GWaveNet (bottom). We present the average training (solid) and validation (yellow) losses (solid line) and accuracies (dashed line) at the default threshold of 0.5. The standard error is calculated at 3 standard deviations σ (shadowed region). The curriculum learning step is shown by vertical dotted lines, and we mark the best-performing epoch out of every step with a red star, i.e. the epoch with the best validation accuracy up to a given tolerance (see Eq. 2).

For **FindCNN** (top panel) we can observe that at the beginning of the first curriculum step, both training and validation losses decrease rapidly, while the accuracy increases, with the best-performing epoch at the end of the step. A similar pattern is observed in the second step. However, by the third step ($f_{max} = 30$ Hz), signs of overfitting emerge, with the best performance occurring at the beginning of the step. Overfitting becomes more pronounced in the fourth and fifth steps, evidenced by the divergence between training and validation loss and accuracy.

Such overfitting is not observed in **GWaveNet**, as training and validation are close together throughout the progressive curriculum learning steps. Additionally, the best-performing epoch typically occurs in the middle or at the end of each step. Note that, due to the early stopping method (see Section 4.3), the curriculum steps are shorter for easier-to-learn datasets, and longer for harder ones. Another notable detail is the expected increase in loss at the beginning of each curriculum learning step, followed by a decrease as learning stabilises, which is characteristic of curriculum learning strategies.

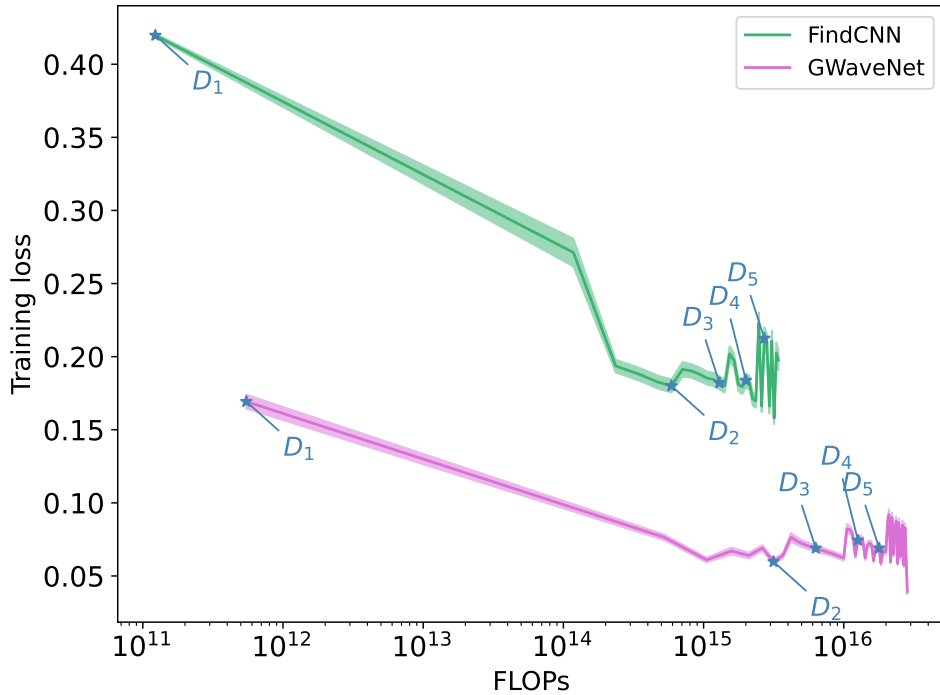


Figure 4. Training losses over the number of floating point operations (FLOPs) in logarithmic scale for **FindCNN** (green) and **GWaveNet** (pink). We present the average loss per epoch for the cumulative amount of the number of FLOPs and 3 standard deviations σ . We mark with a blue star the beginning of each curriculum step.

Based on these observations, we can conclude that **GWaveNet** outperforms **FindCNN** with fewer trainable parameters, potentially implying lower computational cost. In Fig. 4, we present the training loss as a function of the number of floating point

operations (FLOPs) for **FindCNN** (green) and **GWaveNet** (pink), and also mark in blue the beginning of each curriculum step. We can observe that for D_1 and D_2 curriculum steps the learning is smooth as the loss is minimized. However, for the hardest curriculum learning steps the loss becomes quite unstable, particularly D_5 for both models. From this plot, it is evident that **GWaveNet** performs more FLOPs than **FindCNN**, in part because it trains for more epochs, but also since the beginning of the training due to its architecture. Still, **GWaveNet** achieves a better loss reduction with a comparable number of FLOPs.

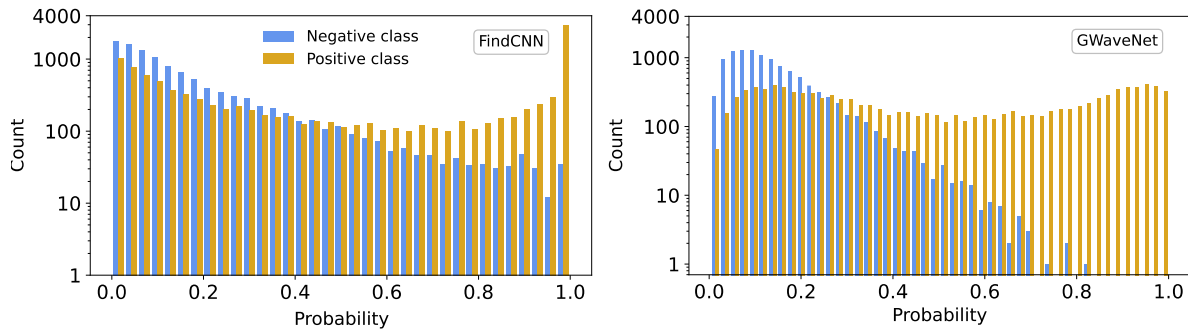


Figure 5. Distribution of the score for if a GW signal is present, as determined by each model. We show the noise class in yellow, and noise + signal class in blue.

While accuracy and loss functions are relevant magnitudes to measure performance, we are interested in minimizing the number of FPs. To assess the separability of both classes, in Fig. 5 we show the noise (negative class, in blue) and the noise + GW signal (positive class, in yellow) of the testing set as a function of the score of if it contains a GW signal. We can observe that **FindCNN** is more decisive than **GWaveNet**, as it usually provides extreme scores, either 0 or 1. Nonetheless, this decisiveness is a symptom of being a “yes-classifier”, as many noise samples are classified with high scores. On the other hand, **GWaveNet** is more conservative and is less keen on providing extreme scores values, a desired behaviour for this particular application. Furthermore, for **GWaveNet** there is a notable separation between both classes for scores > 0.81 . Note that both models use a weighted loss function: **FindCNN** is weighted by 0.4, while **GWaveNet** is weighted by 0.1.

In a GW experiment, it is crucial assess the number of FP. A common metric in GW is the false alarm probability (FAP), also known as false positive rate. In the left-hand panel of Fig. 6 we plot FAP as a function of the decision threshold for **FindCNN** (green) and **GWaveNet** (pink). We mark the target FAP = 1% in red, as defined in [29]. We can observe that **GWaveNet** achieves FAP = 1% for a decision threshold of 0.46, while **FindCNN** needs a more aggressive decision threshold of 0.86. Furthermore, **GWaveNet** allows to set $\text{FAP} \leq 10^{-4}$.

In ML it is standard to use the receiver operator characteristic (ROC) curve, i.e. true positive rate as a function of false positive rate for different decision threshold steps. In the right-hand panel of Fig. 6 we show the ROC curve of **FindCNN** (green)

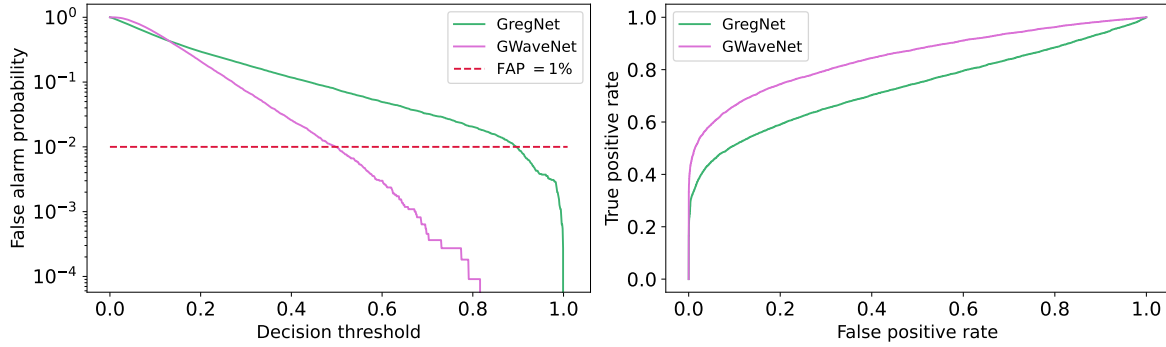


Figure 6. (Left) False alarm probability (FAP) – or false positive rate – in logarithmic scale as a function of the decision threshold for FindCNN (green) and GWaveNet (pink), marking the threshold FAP= 1% in red. (Right) Receiver operator characteristic (ROC) curve of FindCNN (green) and GWaveNet (pink).

and GWaveNet (pink), and we can observe how GWaveNet achieves a larger area under the curve, outperforming FindCNN.

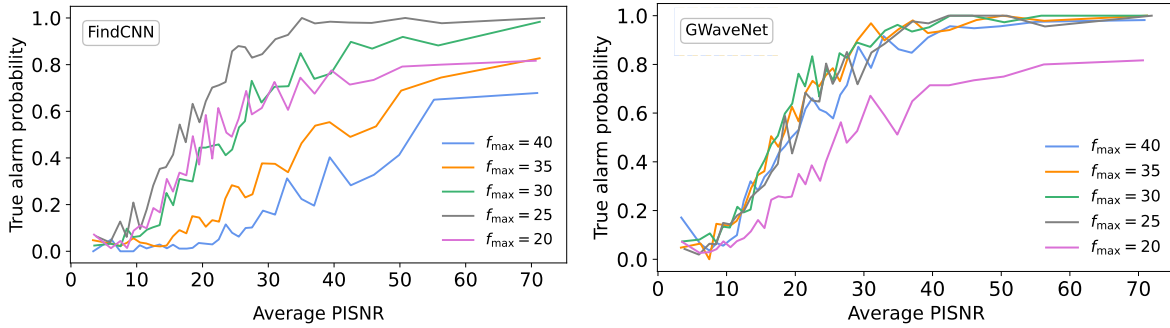


Figure 7. True alarm probability (TAP)-or true positive rate-as a function of PISNR for FindCNN (left) and GWaveNet (right) for different curriculum steps-stepping on average maximum frequency f_{\max} -at false alarm probability (FAP) of 1%.

One of the the main limitations of FindCNN (see Section 2), is that the network forgets the previous curriculum learning steps. To compare the “memory” of FindCNN, we reproduce Fig. 5 of [29] in Fig. 7. Here, we represent the true alarm probability (TAP), also known as the true positive rate, as a function of the average PISNR for the final models after the progressive curriculum learning strategy. In the left-hand panel of Fig. 7, we can see that the final FindCNN has a TAP > 0.5 for signals with $\text{PISNR} > 30$ and $f_{\max} = 20, 25, 30$ Hz, the most difficult samples. As expected, TAP decreases for lower PISNR, which corresponds to the most quiet signals. Nonetheless, its performance drops ~ 20 percentage points (p.p.) for $f_{\max} = 35, 40$ Hz at ≈ 25 PISNR, due to catastrophic forgetting. In a realistic GW search, this would be unreliable, as the algorithm would not alert about the signals closer to the merger. On the other hand, we can observe how the final GWaveNet can “remember” easier data sets while maintaining a comparable performance to FindCNN for the most difficult data set $f_{\max} = 20$ Hz.

As we present in Table 2, **GWaveNet** outperforms **FindCNN** by 10 p.p., but these models are unable to run on an FPGA due to memory limitations. In Table 2 we also show the accuracies of the modified models before and after quantization. See Section 4.4 for further details on memory limitations and quantization strategy. It is relevant to note that **FindCNN2D** and **GWaveNet2D** outperform their 1-dimensional versions by ~ 3 p.p., which could imply that Pytorch [66] is better optimized for vision applications. This could also result in better numerical stability, leading to higher accuracies, but further investigation is needed. On the other hand, the modified versions perform worse than the original ones, due to a simplification in certain operations, such as lowering the size of the dense layers for **FindCNN**, and changing the padding mode, changing the activation functions to linear equivalents and also lowering the size of the dense layers for **GWaveNet**. This is particularly notorious for **GWaveNet2DModified**, which has ~ 5 p.p. less accuracy than original **GWaveNet**, but its performance improves ~ 1 p.p. after quantization, likely due to the smoothing of the possibly overfit learnt manifold. Nonetheless, the worst-performing **GWaveNet** still outperforms the best-performing **FindCNN** by ~ 2 p.p.

Model	Before quantization	After quantization
FindCNN	66.81%	-
FindCNN2D	69.50%	69.37%
FindCNN2DModified	66.70%	65.07%
GWaveNet	76.22%	-
GWaveNet2D	79.42%	77.28%
GWaveNet2DModified	71.72%	72.42%

Table 2. Test accuracies at FAP set at 1% before and after quantization. All models were tested on 22000 samples, except for the **GWaveNet2D** and **GWaveNet2DModified** post-quantization models, which were tested on 5000 samples, due to timeout constraints. We highlight in bold the best **FindCNN** model and the worst **GWaveNet** model.

5.2. Time, energy and economic cost

To compare the models' efficiencies, we measured the time taken to test 22,000 samples on both the CPU and GPU and 1,000 samples on the FPGA. The results of time (ms), energy consumption (mJ), and cost (\$/year) to run each model for CPU, GPU and FPGA are presented in Table 3. As mentioned in Section 4.4, we were unable to compile **GWaveNet** in the FPGA due to software limitations, potentially due to the lack of support of the padding needed for causal convolutions, but further investigation is required.

Regarding the average inference time, we can observe how all **FindCNN** models take ~ 25 ms to predict a sample in CPU and GPU. However, the time in an FPGA is 4

Model	Time (ms)			Energy consumption (mJ)			Economic cost (\$/year)		
	CPU	GPU	FPGA	CPU	GPU	FPGA	CPU	GPU	FPGA
FindCNN	27.53 \pm 3.69	21.75 \pm 1.89	-	107.24 \pm 4.26	617.12 \pm 37.11	-	28.83	210.01	-
FindCNN2D	29.58 \pm 0.10	20.90 \pm 1.56	84.54 \pm 0.10	177.93 \pm 1.60	606.74 \pm 32.06	468.59 \pm 2.40	44.52	214.87	41.03
FindCNN-2DModified	29.54 \pm 0.11	24.87 \pm 1.65	84.28 \pm 0.10	178.35 \pm 1.34	694.59 \pm 28.46	471.51 \pm 2.96	44.69	206.72	41.41
GWaveNet	154.75 \pm 0.38	33.60 \pm 2.76	-	583.66 \pm 5.56	983.83 \pm 60.52	-	27.92	216.72	-
GWaveNet2D	85.28 \pm 2.87	29.41 \pm 1.77	-	568.92 \pm 4.95	858.11 \pm 36.83	-	49.38	215.96	-
GWaveNet-2DModified	65.54 \pm 3.67	26.02 \pm 3.25	-	240.76 \pm 5.85	752.49 \pm 57.90	-	27.19	214.05	-

Table 3. Average time (ms) and energy consumption (mJ) to predict a single sample and economic cost of running each model in a year (\$/year) for different devices (see details in Section 4.1) at 3 standard deviations given 10 experiments. Note that only FindCNN2D and FindCNN2DModified was compatible with our quantization framework.

times longer. Further exploration revealed that the bottleneck was caused by the batch normalization layer in Vitis AI [76]. Ignoring this layer decreased the FPGA times and energy consumption in half. Nonetheless, the lack of speed of the FPGA could be due to our particular low-end FPGA, which was not designed for processing high-dimensional time series data.

For **GWaveNet**, the inference time on GPU is slightly higher than **FindCNN**, taking 1.5 times longer. Notably, on the CPU, original **GWaveNet** takes ~ 2 times more than the 2-dimensional versions, making **GWaveNet2DModified** the fastest, due to its simplified nature. It is also interesting to note that on the GPU the original models are slightly slower than their 2-dimensional equivalents. As we hypothesized in the previous section, this could be attributed to PyTorch’s enhanced optimization for vision applications. However, it is worth noting that, given the input duration of 300 s, the time consumption of all the models is remarkably low.

Regarding the energy consumption needed for inference (see Table 3), when comparing the same model across various devices, we can see that while the GPU is one of the fastest, it is also the one that consumes the most energy. As before, if we ignore the batch normalization layers of **FindCNN** models on the FPGA, the energy consumption is halved, being comparable to the CPU consumption. Thus, we believe that a model fully optimized for an FPGA would have a better energy performance, and this will be explored in future works.

In a realistic situation, these models would run through the whole observing run. In Table 3, we consider the economic cost of running the models for a year, taking the average industry electricity price in the USA, as most GW clusters are there. In 2022, the average electricity cost was 0.0845 \$/kWh [77]. As expected, the GPU is the most expensive. On the other hand, the cost of running on an FPGA is $\approx 7\%$ cheaper than running on a CPU. Note that we only take into account the electricity prices, but adding the upfront and upkeep prices of the devices, the FPGA is by far the least expensive. Assuming the price at launch date over the number of lifetime years, under heavy use, and the prices for running **FindCNN2D** for a year, running on a CPU ($\approx 495\$$) or GPU ($\approx 465\$$) have similar expenses, whereas running on an FPGA ($\approx 65\$$) costs over seven

times less.

Lastly, running `FindCNN` and `GWaveNet` incurs comparable economic costs. This highlights `GWaveNet`'s efficiency, achieving better performance without significantly increasing computational resources, making it a more cost-effective model for ML-based BNS search algorithms.

6. Conclusions

In this work, we developed a novel ML-based GW detection algorithm for the early inspiral of BNS mergers, `GWaveNet`, inspired by the audio generating `WaveNet` [65]. We compare its performance to the current state-of-the-art, `FindCNN` [29], reproducing this work in simulated detector noise from the third observing run. Moreover, we compare their time, energy consumption and cost in CPU, GPU and FPGA.

As in [29], we implement a progressive curriculum learning strategy, where easier (more difficult) samples have higher (lower) maximum frequency f_{max} , and are closer (further) to the merger, meaning that they will be detected later (earlier). Both `FindCNN` and `GWaveNet` are binary classifiers, that differentiate between noise (negative class) and noise + signal (positive class) solely utilizing the inspiral of BNS mergers.

`GWaveNet` has less trainable parameters than `FindCNN`, but it is deeper and more complex, implementing key ideas to improve its performance at a limited computational cost. Furthermore, we implement a more flexible training strategy, accommodating `GWaveNet` to the difficulty of each curriculum step. In terms of accuracy at FAP=1%, `FindCNN` achieves 66.81%, while `GWaveNet` achieves 76.22%, outperforming `FindCNN` by ~ 10 p.p. In terms of inference time, `FindCNN` is ~ 2 ms faster on GPU, but we believe `GWaveNet` is the preferred model due to its enhanced performance.

Regarding the FPGA, while we were able to test the performance of `FindCNN`, this was not possible with `GWaveNet` due to software limitations. In terms of costs, the FPGA is the most sustainable option. Although the GPU is the fastest device, it also has the highest energy consumption.

The present work demonstrated high performance in terms of accuracy at a limited computational cost. In future works, we will study more realistic scenarios, moving to real detector data. Furthermore, other FPGA software and/or hardware, better fitting for our application, could also be explored.

Acknowledgments

The authors thank M. Hester and R. Aaij for the fruitful and inspiring discussions during this study. This project was supported by Nikhef Laboratory, and the authors extend their gratitude to the Nikhef computing group. This publication is part of the project Computing for Virgo with file number 2023.033 which is financed by the Dutch Research Council (NWO). M.L. is supported by the research program of the Netherlands Organisation for Scientific Research (NWO). MvdS acknowledges support

from the European Union, AHEAD 2020 (grant number 871158). This publication is part of the project Cortex with project number 00686766 of the research programme NWA which is (partly) financed by the Dutch Research Council (NWO). This material is based upon work supported by NSF's LIGO Laboratory which is a major facility fully funded by the National Science Foundation.

References

- [1] J. Aasi et al. 2015 *Class. Quant. Grav.* **32** 074001
- [2] F. Acernese et al. 2015 *Class. Quant. Grav.* **32** 024001
- [3] B. P. Abbott et al. 2016 *Phys. Rev. Lett.* **116** 061102
- [4] B. P. Abbott et al. 2019 *Phys. Rev. X* **9** 031040
- [5] R. Abbott et al. 2021 *Phys. Rev. X* **11** 021053
- [6] R. Abbott et al. 2024 *Phys. Rev. D* **109** 022001
- [7] R. Abbott et al. 2023 *Phys. Rev. X* **13** 041039
- [8] B. P. Abbott et al. 2017 *Phys. Rev. Lett.* **119** 161101
- [9] M. Punturo et al. 2010 *Class. Quant. Grav.* **27** 194002
- [10] D. Reitze et al. 2019 *Bull. Am. Astron. Soc.* **51** 035
- [11] P. Amaro-Seoane et al. 2017 *arXiv e-prints* 1702.00786
- [12] F. Iacovelli, M. Mancarella, S. Foffa, and M. Maggiore 2022 *Astrophys. J.* **941** 208
- [13] V. Kalogera et al. 2021 *arXiv e-prints* 2111.06990
- [14] L. Baiotti, I. Hawke, L. Rezzolla, and E. Schnetter 2005 *Phys. Rev. Lett.* **94** 131101
- [15] C. Messick et al. 2017 *Phys. Rev. D* **95** 042001
- [16] S. Sachdev et al. 2019 *arXiv e-prints* 1901.08580
- [17] L. Tsukada et al. 2023 *Phys. Rev. D* **108** 043004
- [18] S. A. Usman et al. 2016 *Classical and Quantum Gravity* **33** 215004
- [19] B. Allen, W. G. Anderson, P. R. Brady, D. A. Brown, and J. D. E. Creighton 2012 *Phys. Rev. D* **85** 122006
- [20] S. Sachdev et al. 2020 *Astrophys. J. Lett.* **905** L25
- [21] A. H. Nitz, M. Schäfer, and T. D. Canton 2020 *The Astrophysical Journal Letters* **902** L29
- [22] R. Magee et al. 2021 *Astrophys. J. Lett.* **910** L21
- [23] M. Kovalam, M. A. K. Patwary, A. K. Sreekumar, L. Wen, F. H. Panther, and Q. Chu 2022 *The Astrophysical Journal Letters* **927** L9
- [24] S. S. Chaudhary et al. 2024 *Proc. Nat. Acad. Sci.* **121** e2316474121
- [25] M. Asch et al. 2018 *International Journal of High Performance Computing Applications* **32** 435–479

- [26] J. Aveiro, F. F. Freitas, M. Ferreira, A. Onofre, C. Providênci, G. Gonçalves, and J. A. Font 2022 *Physical Review D* **106**
- [27] B. Liu, D. Zydek, H. Selvaraj, and L. Gewali. In: *2012 13th International Conference on Parallel and Distributed Computing, Applications and Technologies*. 2012, 337–342.
- [28] G. Baltus, J. Janquart, M. Lopez, A. Reza, S. Caudill, and J.-R. Cudell 2021 *Phys. Rev. D* **103** 102003
- [29] G. Baltus, J. Janquart, M. Lopez, H. Narola, and J.-R. Cudell 2022 *Phys. Rev. D* **106** 042002
- [30] M. Cavaglia, S. Gaudio, T. Hansen, K. Staats, M. Szczepanczyk, and M. Zanolin 2020 *arXiv e-prints* 2002.04591
- [31] M. L. Portilla, I. D. Palma, M. Drago, P. Cerdá-Duran, and F. Ricci 2021 *Phys. Rev. D* **103** 063011
- [32] M. López, M. Drago, I. D. Palma, F. Ricci, and P. Cerdá-Durán. In: *2021 International Conference on Content-Based Multimedia Indexing (CBMI)*. 2021, 1–6.
- [33] Q. Meijer, M. Lopez, D. Tsuna, and S. Caudill 2024 *Phys. Rev. D* **109** 022006
- [34] V. Boudart and M. Fays 2022 *Phys. Rev. D* **105** 083007
- [35] V. Boudart 2023 *Phys. Rev. D* **107** 024007
- [36] S. Bahaadini, V. Noroozi, N. Rohani, S. Coughlin, M. Zevin, J. Smith, V. Kalogera, and A. Katsaggelos 2018 *Information Sciences* **444** 172–186
- [37] P. Laguna et al. 2024 *Classical and Quantum Gravity* **41** 055004
- [38] M. Lopez, V. Boudart, K. Buijsman, A. Reza, and S. Caudill 2022 *Phys. Rev. D* **106** 023027
- [39] M. Lopez, V. Boudart, S. Schmidt, and S. Caudill 2022 *arXiv pre-print* 2205.09204
- [40] T. Dooney, S. Bromuri, and L. Curier. In: *2022 IEEE International Conference on Big Data (Big Data)*. Los Alamitos, CA, USA: IEEE Computer Society, Dec. 2022, 5468–5477.
- [41] T. Dooney, R. L. Curier, D. S. Tan, M. Lopez, C. Van Den Broeck, and S. Bromuri 2024 *Phys. Rev. D* **110** 022004
- [42] E. Cuoco et al. 2021 *Mach. Learn. Sci. Tech.* **2** 011002
- [43] K. He, X. Zhang, S. Ren, and J. Sun 2015 *arXiv e-prints* 1512.03385
- [44] W. Wei and E. A. Huerta 2021 *Phys. Lett. B* **816** 136185
- [45] G. Baltus, J. Janquart, M. Lopez, A. Reza, S. Caudill, and J.-R. Cudell. In: *2021 International Conference on Content-Based Multimedia Indexing (CBMI)*. 2021, 1–6.
- [46] W. Wei, E. A. Huerta, M. Yun, N. Loutrel, M. A. Shaikh, P. Kumar, R. Haas, and V. Kindratenko 2021 *Astrophys. J.* **919** 82

- [47] H. Yu, R. X. Adhikari, R. Magee, S. Sachdev, and Y. Chen 2021 *Phys. Rev. D* **104** 062004
- [48] R. Alfaidi and C. Messenger 2024 *arXiv e-prints* 2402.04589
- [49] W. van Straalen, A. Kolmus, J. Janquart, and C. V. D. Broeck 2024 *arXiv e-prints* 2407.10263
- [50] W. Wei, A. Khan, E. A. Huerta, X. Huang, and M. Tian 2021 *Physics Letters B* **812** 136029
- [51] R. Sang, Q. Liu, and Q. Zhang. In: *2016 IEEE MTT-S International Conference on Numerical Electromagnetic and Multiphysics Modeling and Optimization (NEMO)*. 2016, 1–2.
- [52] E. E. Khoda et al. 2023 *Mach. Learn. Sci. Tech.* **4** 025004
- [53] Z. Que, H. Fan, M. Loo, H. Li, M. Blott, M. Pierini, A. Tapper, and W. Luk 2024 *ACM Transactions on Embedded Computing Systems* **23** 1–28
- [54] Z. Que et al. In: *32nd IEEE International Conference on Application-specific Systems, Architectures and Processors*. June 2021. arXiv: 2106.14089 [cs.LG].
- [55] C. M. Biwer, C. D. Capano, S. De, M. Cabero, D. A. Brown, A. H. Nitz, and V. Raymond 2019 *Publications of the Astronomical Society of the Pacific* **131** 024503
- [56] R. Abbott et al. 2023 *Astrophys. J. Suppl.* **267** 29
- [57] A. Buonanno, Y. Chen, and M. Vallisneri 2003 *Phys. Rev. D* **67** 104025
- [58] A. Akhshi, H. Alimohammadi, S. Baghram, S. Rahvar, M. R. R. Tabar, and H. Arfaei 2020 *arXiv pre-print* 2005.11352
- [59] U. Gupta, Y. G. Kim, S. Lee, J. Tse, H.-H. S. Lee, G.-Y. Wei, D. Brooks, and C.-J. Wu. In: *2021 IEEE International Symposium on High-Performance Computer Architecture (HPCA)*. 2021, 854–867.
- [60] M. N. Office. *How can we reduce the carbon footprint of global computing?* <https://news.mit.edu/2022/how-can-we-reduce-carbon-footprint-global-computing-0428>. Accessed 10 June 2024. 2022.
- [61] TechPowerUp. *AMD EPYC 7551P*. <https://www.techpowerup.com/cpu-specs/epyc-7551p.c1929>. Accessed 23 June 2024. 2024.
- [62] Microway, Inc. *NVIDIA Tesla V100 Price Analysis*. <https://www.microway.com/hpc-tech-tips/nvidia-tesla-v100-price-analysis/>. Accessed 09 June 2024. 2018.
- [63] NVIDIA. *GeForce GTX 1080 Specifications*. <https://www.nvidia.com/en-gb/geforce/graphics-cards/geforce-gtx-1080/specifications/>. Accessed 09 June 2024. 2024.
- [64] Advanced Micro Devices, Inc. *AMD Kria KV260 Vision Starter Kit*. Accessed 27 March 2024.

- [65] A. van den Oord, S. Dieleman, H. Zen, K. Simonyan, O. Vinyals, A. Graves, N. Kalchbrenner, A. Senior, and K. Kavukcuoglu 2016 *arXiv e-prints* arXiv:1609.03499
- [66] A. Paszke et al. 2019 *arXiv e-prints* 1912.01703
- [67] PyTorch. *PyTorch Documentation - torch.nn.BCEWithLogitsLoss*. Accessed 24 April 2024.
- [68] S. Ioffe and C. Szegedy 2015 *arXiv e-prints* 1502.03167
- [69] V. Nair and G. E. Hinton. In: *Proceedings of the 27th International Conference on International Conference on Machine Learning*. ICML'10. Haifa, Israel: Omnipress, 2010, 807–814.
- [70] PyTorch. *PyTorch Documentation - torch.nn.MaxPool1d*. Accessed 22 April 2024.
- [71] A. van den Oord, N. Kalchbrenner, O. Vinyals, L. Espeholt, A. Graves, and K. Kavukcuoglu 2016 *arXiv e-prints* arXiv:1606.05328
- [72] D. P. Kingma and J. Ba 2017 *arXiv e-prints* 1412.6980
- [73] Advanced Micro Devices, Inc. *AMD Vitis AI Documentation*. Accessed 02 April 2024.
- [74] D. Miyashita, E. H. Lee, and B. Murmann 2016 *arXiv e-prints* 1603.01025
- [75] Xilinx, Inc. *Vitis-AI Quantization Configuration*. Accessed 07 May 2024.
- [76] Advanced Micro Devices, Inc. *AMD Vitis AI Documentation - Operators Supported by PyTorch*. Accessed 2024.
- [77] Statista. *Energy Prices in the U.S.* <https://www.statista.com/topics/6337/energy-prices-in-the-us/#topicOverview>. Accessed 23 June 2024. 2024.